inorganics

MDPI

Article

Manganese(II) Bromide Compound with Diprotonated 1-Hydroxy-2-(pyridin-2-yl)-4,5,6,7-tetrahydrobenzimidazole: Dual Emission and the Effect of Proton Transfers

Alexey S. Berezin [1,*], Boris Selivanov [2], Andrey Danilenko [1], Aleksandr Sukhikh [1] and Andrey Komarovskikh [1]

[1] Nikolaev Institute of Inorganic Chemistry SB RAS, Acad. Lavrentiev Ave. 3, 630090 Novosibirsk, Russia
[2] Vorozhtsov Novosibirsk Institute of Organic Chemistry SB RAS, Acad. Lavrentiev Ave. 9, 630090 Novosibirsk, Russia
* Correspondence: berezin-1991@ngs.ru or berezin@niic.nsc.ru

Abstract: An organic–inorganic cation–anion manganese(II) tetrabromide compound with diprotonated 1-hydroxy-2-(pyridin-2-yl)-4,5,6,7-tetrahydrobenzimidazole, $[H_3L][MnBr_4][H_2O]$, has been synthesized and investigated. The compound has a few possible pathways for proton transfers, which play an important role in the observed luminescence, optical, and magnetic properties. The proton transfers result in the appearance of two-band luminescence. One band is caused by the Mn(II) *d-d* transitions. The other band is caused by the transition from the triplet state of organic cation and the *d-d* transition of manganese(II) coupled through $\{[H_3L]\}$-$\{[MnBr_4]\}$-$\{[H_2O]\}$ vibrations. The optical absorption spectra of $[H_3L][MnBr_4][H_2O]$ indicate the presence of two direct and one indirect band transitions. The reason for the two-band luminescence and complex optical absorption in $[H_3L][MnBr_4][H_2O]$ were additionally considered using the DFT calculations.

Keywords: manganese(II); luminescence; optics; EPR; proton transfer; DFT

check for updates

Citation: Berezin, A.S.; Selivanov, B.; Danilenko, A.; Sukhikh, A.; Komarovskikh, A. Manganese(II) Bromide Compound with Diprotonated 1-Hydroxy-2-(pyridin-2-yl)-4,5,6,7-tetrahydrobenzimidazole: Dual Emission and the Effect of Proton Transfers. *Inorganics* **2022**, *10*, 245. https://doi.org/10.3390/inorganics10120245

Academic Editor: Kazuyuki Takahashi

Received: 24 October 2022
Accepted: 30 November 2022
Published: 6 December 2022

Publisher's Note: MDPI stays neutral with regard to jurisdictional claims in published maps and institutional affiliations.

Copyright: © 2022 by the authors. Licensee MDPI, Basel, Switzerland. This article is an open access article distributed under the terms and conditions of the Creative Commons Attribution (CC BY) license (https://creativecommons.org/licenses/by/4.0/).

1. Introduction

Luminescent manganese(II) complexes have been extensively studied over the past few decades on account of their intriguing optical, thermal, and magnetic properties [1–15]. Their potential use as multifunctional materials attracts special attention. The luminescence of the manganese(II) complexes commonly originates from the Mn(II) spin-forbidden $d\text{-}d\ ^4T_1(\mathbf{G}) \rightarrow {}^6A_1(\mathbf{S})$ transition [16,17]. The emission energy of the Mn(II) center is known to be strongly dependent on the crystal field parameters [18,19] and varies from green to near-infrared for the tetrahedral and octahedral crystal fields, respectively [20–23]. The metal-perturbed intraligand transition can also result in the luminescence of Mn(II) complexes, but such luminescence is still only rarely observed [24]. The combination of these two mechanisms in one compound can result in the observation of multiband luminescence, which has been one of the special goals in material science [25].

The organic–inorganic tetrahalomanganate(II) compounds are of great interest because they can exhibit bright green luminescence with high quantum yields. It is worth noting that the interaction between organic cations and tetrahalomanganate(II) anions occurs through noncovalent interactions and hydrogen bonds [26,27]. These interactions play an important role in the possibilities of the energy and charge transfer between cations and anions in both directions and the proton transfer processes. This can provide multiband luminescence on account of the different kinds of transfers and allows the obtaining of dynamic systems by tautomerism type. It should be noted that the systems with proton transfers, being able to tautomerize in the ground (GSIPT) or excited states (ESIPT), are actively investigated nowadays because of their ability to simultaneously manifest optical, magnetic, and other properties corresponding to few tautomeric states [28]. Such systems

can be used for the creation of photonic switches, molecular logic gates, photochromic memory devices, and white-light emission diodes [29,30]. The study of the compounds based on the proton transfer organic moiety and manganese(II) ions can result in the emergence of new unique systems with combined interesting optical, luminescence, and magnetic properties.

Herein, the synthesis and investigation of the optical, luminescence, and magnetic properties of the organic–inorganic tetrabromomanganate(II) compound, $[H_3L][MnBr_4][H_2O]$ with 1-hydroxy-2-(pyridin-2-yl)-4,5,6,7-tetrahydrobenzimidazole (HL) [31], are reported. The compound exhibits complex absorption behavior, which is probably related to the possibility of intra- and intermolecular proton transfers. The compound demonstrates a two-band photoluminescence with maxima in "green" and "red" ranges that is relevant for the creation of a white-light emission diode based on a blue light source. The electron paramagnetic resonance, low-temperature absorption and photoluminescence measurements supported by DFT calculations were carried out to investigate the mechanisms of absorption and photoluminescence of the obtained compound. The performed investigation expands a class of organic–inorganic manganese(II) compounds having two-band luminescence both in "green" and "red" ranges and can help to understand the nature of this phenomenon.

2. Experimental Work

2.1. Synthesis and Characterization

$[H_3L][MnBr_4][H_2O]$ (1)

The $MnCO_3 \cdot xH_2O$ (44–46% mass Mn) (0.025 g, 0.2 mmol) and 1-hydroxy-2-(pyridin-2-yl)-4,5,6,7-tetrahydrobenzimidazole (HL) (0.043 g, 0.2 mmol) were dissolved together in 3 mL of concentrated hydrobromic acid (48%) (Scheme 1). The solution was stirred at 50 °C (323 K) for 1 h, and the solution was then left to evaporate at room temperature. The formed brownish-yellow crystals were washed by twice decantation with 0.5 mL of cold 0 °C (273 K) hydrobromic acid and dried in the air. Yield: 0.102 g (81%). Anal. Calcd for $C_{12}H_{17}Br_4N_3O_2Mn$(%): C, 23.6; H, 2.8; N, 6.9. Found: C, 23.7; H, 2.7; N, 6.8. X-ray powder diffraction, calorimetric measurements, and IR spectrum are available in ESI.

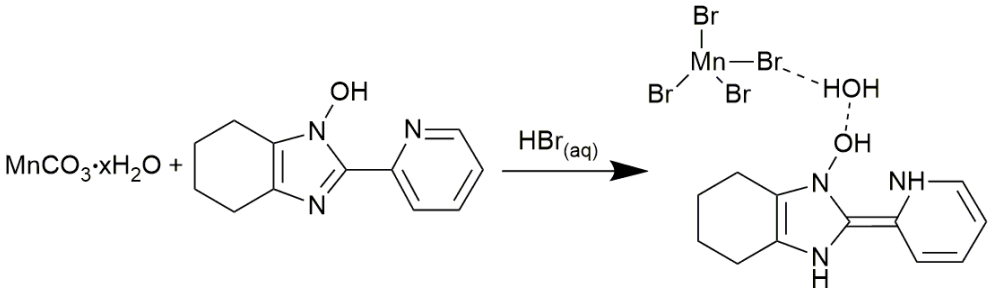

Scheme 1. Synthesis of **1**.

2.2. Methods

Single-crystal X-ray data were collected on a Bruker X8 single-crystal diffractometer equipped with Mo-anode Incoatec IμS 3.0 microfocus X-ray source (λ = 0.71073 Å) and PHOTON III C14 CPAD detector. A standard data collection strategy with φ and ω scans and 0.5° frame width was used. A suitable crystal of **1** was mounted onto the nylon loop with liquid epoxy resin. The sample temperature was kept at 150 K by Oxford Cryosystems Cryostream 800 Plus open-flow nitrogen cooler. Apex3 v.2018-7.2 software package (SAINT, SADABS, RLATT) [32] was used for unit cell determination, calculation of data acquisition strategy, integration, and absorption correction. The hkl datasets were obtained in Olex2 v.1.5 [33] software, using SHELXT v.2018/2 [34] for structure solution and SHELXL v.2018/3 [35] for subsequent refinement. All non-hydrogen atoms were refined anisotropically. Hydrogen atom positions were calculated geometrically and refined using the riding model. CCDC 2214547 contains the supplementary crystallographic data for this

paper. These data can be obtained free of charge from The Cambridge Crystallographic Data Center at www.ccdc.cam.ac.uk/structures.

The PXRD pattern of the bulk sample powder was recorded at room temperature using Bruker D8 Advance powder diffractometer (Cu-anode sealed tube λ = 1.54187Å 40 mA @ 40 kV, Bragg-Brentano scheme with vertical θ-θ goniometer, 0.01023° scan step, LYNXEYE XE-T compound silicon strip detector, motorized divergence slit in fixed sample illumination area mode).

Corrected luminescence spectra were recorded on a Fluorolog 3 spectrometer (Horiba Jobin Yvon) with a cooled PC177CE-010 photon detection module equipped with an R2658 photomultiplier; with continuous 450 W and pulsed (pulse time FWHM 3 μs) 50 W Xe-lamps; and with two Czerny–Turner double monochromators. Absolute values of quantum yields were recorded using the Quanta-φ device of Fluorolog 3. Temperature dependencies of luminescence were studied using Optistat DN optical cryostat (Oxford Instruments). The luminescence quantum yield at 77 K was obtained relative to the quantum yield of the same sample at 300 K [26].

EPR spectra were recorded on the Varian E-109 spectrometer in Q-band at 300 K. A 2,2-diphenyl-1-picrylhydrazyl (DPPH) standard sample was used to calibrate the magnetic field of the spectrometer. The spectrum was simulated in MATLAB (The MathWorks Inc., Natick, MA, USA) using the EasySpin program package for EPR [36].

The structure of the compound was optimized by a spin-unrestricted DFT method using the Amsterdam density functional (BAND) [37,38] program with a gradient exchange functional GGA (BP86 [39,40]). Triple zeta polarized (TZP) basis sets and the no frozen core and Scalar ZORA [41–43] approximations were used in all calculations. The initial positions of atoms were taken from the X-ray structure analysis. The frequency analysis (phonons calculation) was carried out to check the nature of the stationary points (BP86, TZP). The calculation of the *g*-tensor [44] was performed with a hybrid functional PBE0 [45,46]. The electronic excitations were calculated using the TD-DFT method [47,48] (BP86 and CAM-B3LYP [49], TZP) and additionally with the spin-flip approximation [50,51] (BP86 and CAM-B3LYP, TZP). The zero-field splitting (ZFS) tensor was calculated for $[MnBr_4]^{2-}$ and $[MnBr_4H]^{1-}$ fragments cut from the structure of (**1**) in global and local minima on the potential energy surface (PES), respectively. The spin–spin and spin–orbit parts of the D were calculated using the approaches implemented by [52,53] in the ORCA 5.0 [54–56] package. The unrestricted calculations were performed with scalar relativistic ZORA Hamiltonian; the spin–orbit coupling was treated using the spin–orbit mean-field (SOMF) method [57]. The hybrid PBE0 functional [58] and full-electron relativistic basis sets def2-TZVP [59] for all atoms were employed.

FT-IR spectra were recorded on a Bruker Vertex 80 spectrometer at ambient temperature.

Elemental analysis (C, H, and N) was performed on a Carlo–Erba analyzer using standard technique.

Differential scanning calorimetric measurements were performed using a heat flow measurement method using a Netzsch TG 209 F1 calorimeter with a heating rate of 10 K min^{-1}, in a He flow of 30 mL min^{-1}.

3. Results and Discussion

3.1. Synthesis and Characterization

The single-crystal X-ray diffraction analysis reveals that compound **1** crystallizes in the $P2_1/c$ space group with $Z = 4$ and $Z' = 1$ (Table S1). The symmetrically independent fragment contains twice protonated $[H_3L]^{2+}$ cations, $[MnBr_4]^{2-}$ anions, and crystallized $[H_2O]$ molecules. The Mn(II) ion coordination geometry is a distorted tetrahedron (Figure 1) by four bromides with the Mn-Br distances (and Br-Mn-Br angles) varying in the range of R(Mn-Br) = 2.481–2.539Å (φ(Br-Mn-Br) = 101.8–116.8°) (Tables S2–S7). Each isolated $[MnBr_4]^{2-}$ anion is surrounded by two $[H_2O]$ molecules and six $[H_3L]^{2+}$ cations. Each $[H_2O]$ molecule is connected with two $[MnBr_4]^{2-}$ anions through the OH_{water} ... Br(Mn) ($R(OH_{water}\text{-}Br_1)$ = 3.256Å and $R(OH_{water}\text{-}Br_2)$ = 3.367Å) interactions, with two $[H_3L]^{2+}$

cations through the $OH_{hydroxy} \ldots O_{water}H$ ($R(OH_{hydroxy} \ldots O_{water})$ = 2.498Å), and with $CH \ldots O_{water}$ ($R(CH_{benzim} \ldots O_{water})$ = 2.498Å) interactions. Each $[H_3L]^{2+}$ cation is connected with $[MnBr_4]^{2-}$ anions through the $NH_{imid} \ldots Br(Mn)$ ($R(NH_{imid}{}^1 \ldots Br)$ = 3.309 Å and $R(NH_{imid}{}^2\text{-}Br)$ = 3.345 Å). The non-covalent interactions and hydrogen bonds in (**1**) form a 3D framework of intermolecular contacts. The $[H_3L]^{2+}$ cation also contains intramolecular $NH_{pyr} \ldots O_{hydroxy}$ interaction with $R(NH_{pyr} \ldots O_{hydroxy})$ = 2.743Å, which binds together imidazone and pyridine rings, resulting in a relatively small torsion angle of 2.69° between two aromatic rings. The short $NH_{pyr} \ldots O_{hydroxy}$ distance together with the abovementioned $OH_{water} \ldots Br(Mn)$ and $OH_{hydroxy} \ldots O_{water}H$ interactions make it possible for an intra- and intermolecular proton transfer (Figures S1 and S18–S28) resulting in the hypothetically seven tautomers.

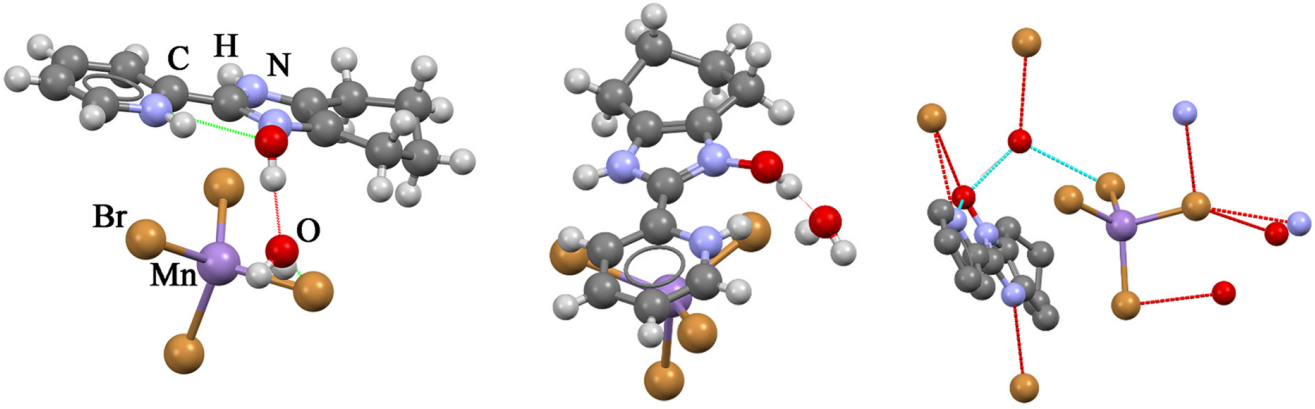

Figure 1. Structure of $[H_3L][MnBr_4][H_2O]$ moiety of **1:** (**a**) against and (**b**) along [112] directions; and (**c**) along [100] with omitted hydrogen atoms. The hydrogen bonds presented by red, green, and cyan lines.

The calorimetric measurements show that the obtained compound is thermally stable up to 80 °C (353 K) (Figure S3). The mass loss in the temperature range of 80 °C (353 K)–150 °C (423 K) is approximately equal to 3.5% which is close to 3% of the mass abundance of $[H_2O]$ fragment in the $[H_3L][MnBr_4][H_2O]$ compound (Table S8). The loss of the $[H_2O]$ fragment is also confirmed by the calorimetric method combined with the mass spectrometry technique (Figure S3). In the temperature range of 200 °C (473 K)–370 °C (643 K), an additional mass loss of approximately 27% is observed. It can be assumed that the remaining $[H_3L][MnBr_4]$ fragment loses the Br_2 or two HBr fragments (27% of the mass abundance). The presence of the two temperature peaks in the DSC curve can indicate that the two HBr fragments are lost.

The IR spectrum of **1** consists of narrow lines set from 500 cm^{-1} to 1700 cm^{-1} corresponding to the organic cation vibrations. The positions and relative intensities of the lines are slightly different from the lines of the organic HL compound (Figure S4). The IR spectrum of **1** in the range of 2200–3500 cm^{-1} consists of a set of broad bands which can be attributed to the X-H and X-H … Y vibrations. The IR spectrum of HL in the same range consists of three narrow lines corresponding to the X-H vibrations and one broadband at 2400 cm^{-1} corresponding to the N-H … O vibration. The significantly greater number of vibration bands in **1** than in free HL can be explained by the addition of the $OH_{hydroxy} \ldots O_{water}H$, $NH_{imid} \ldots Br(Mn)$, and two $OH_{water} \ldots Br(Mn)$ vibrations (Figures S4 and S11–S15). The quantum chemical calculated IR spectrum of **1** is in good agreement with the experimental data. According to the calculated data, the broadening of the high energy band is caused by the possible intra- and intermolecular proton transfer (Figures S11–S15). At the same time, only the $NH_{pyr} \ldots O_{hydroxy}$ proton transfer can be realized in HL, corresponding to the 2400 cm^{-1} energy.

3.2. Luminescence

Solid **1** exhibits multi-band photoluminescence in the visible region (Figure 2). The photophysical data are collected in Table 1. The luminescence spectrum of **1** consists of two bands with maxima at λ_1 = 670 nm (1.85 eV) and λ_2 = 538 nm (2.30 eV). Cooling from 300 K to 77 K results in a narrowing of the spectral lines and an up to a ≈90-fold increase in the total photoluminescence integral intensity. The temperature dependence of the λ_1 band photoluminescence integral intensity (Figure 3) not being monotonous with a maximum at a temperature of approximately 100 K can be ascribed to two competing mechanisms. The first mechanism is a thermal population with $\Delta E_{\lambda_1 pop} \approx -35$ meV and the second mechanism is a thermal depopulation with $\Delta E_{\lambda_1 depop} \approx 126$ meV. At the same time, the monotonic temperature dependence of the photoluminescence integral intensity (Figure 3) of the λ_2 band can also be ascribed to two mechanisms. In this case, both mechanisms are thermal depopulations with $\Delta E_{\lambda_2 depop_1} \approx 35$ meV and $\Delta E_{\lambda_2 depop_2} \approx 160$ meV. The equality of the $\Delta E_{\lambda_1 pop}$ and $\Delta E_{\lambda_2 depop_1}$ values indicates the probable interdependence of the λ_1 and λ_2 bands. The temperature dependence of luminescence linewidth of both bands can be fitted to a model with an exciton–optical phonon coupling [60]:

$$w_{\lambda_i} = 2 * E_{p_i} * \sqrt[2]{S_i * \coth\left(\frac{E_{p_i}}{2 * k_B * T}\right)} + w^0_{\lambda_i},$$

where k_B is the Boltzmann constant, $w^0_{\lambda_i}$ is a temperature-independent term, $E_{p_1} \approx 33$ meV and $E_{p_2} \approx 29$ meV are the phonon energies, and $S_1 \approx 20$ and $S_2 \approx 7$ are Huang–Rhys factors. It should be noted that the abovementioned approach for the determination of the phonon energy of **1** gives an error of 5 meV that is greater than $\frac{|E_{p_1} - E_{p_2}|}{2}$. According to the obtained data, the Stokes shifts are $\Delta E_{S_1} \approx 1.29$ eV and $\Delta E_{S_2} \approx 0.38$ eV and the corresponding absorption energies are $\lambda_1^{abs} \approx 3.14$ eV (394 nm) and $\lambda_2^{abs} \approx 2.68$ eV (463 nm). The photoluminescence excitation spectrum for the λ_2 band of **1** consists of partially resolved lines which allow us to determine the crystal field $10Dq$ and Racah parameters B. The analysis of the excitation spectrum using the Tanabe–Sugano approach [61] gives values of $10Dq_{tet}$ = 1810 cm^{-1} and B = 634 cm^{-1} ($10Dq_{tet}/B$ = 2.85). The value of the three lowest excitation energies are $\lambda_2^{Ex_1}$ = 478 nm (2.59 eV), $\lambda_2^{Ex_2}$ = 455 nm (2.73 eV), and $\lambda_2^{Ex_3}$ = 437 nm (2.83 eV). The photoluminescence excitation spectrum for the λ_1 band consists of broadened lines of the λ_2 band and well-resolved lines with energies $\lambda_1^{Ex_1}$ = 510 nm (2.43 eV) and $\lambda_1^{Ex_2}$ = 398 nm (3.12 eV). The luminescence kinetic curves are fitted by the single exponential decay at each temperature. The temperature dependence of τ was fitted to the following equation (Figure 3):

$$\tau(T) = \tau_0/(1 + C * \exp\left(-\frac{\Delta E}{T}\right)),$$

where τ_0 is a radiative lifetime at 0 K, C is a dimensionless parameter, and ΔE is thermal quenching activation energy with $\Delta E \approx 35$ meV for the λ_2 band. It should be noted that the luminescence lifetimes for both bands are equal at 77 K. Based on obtained data, the λ_2 band can be attributed to the *d-d* spin-forbidden manganese(II) transition. At the same time, two different possible mechanisms can be postulated for the λ_1 band. The λ_1 band can originate from the transition from the triplet state of organic cation and from the *d-d* spin-forbidden manganese(II) transition which changed state due to the {[H_2L]-[H_2O]-H-[$MnBr_4$]} vibrations. Moreover, the excitation transfer between the anion and triplet state of organic cation directly or through the {[H_2O]} fragment is possible. The proposed mechanisms of luminescence based on luminescence data and optical data supported by quantum chemical calculations (see below) are presented in Figure 4.

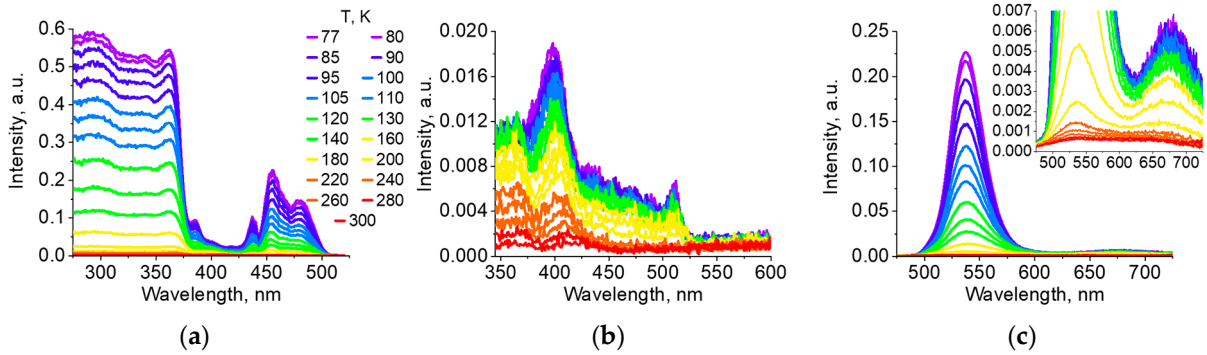

Figure 2. Temperature dependences—of the photoluminescence excitation spectra of (**1**)**:** (**a**) λ_{Em} = 538 nm, (**b**) λ_{Em} = 670 nm ; and of its photoluminescence spectra (**c**) λ_{Ex} = 455 nm.

Table 1. Photophysical data for the polycrystalline compound **1**.

	1
λ_{max} (300 K) [nm] [a]	535
T (300 K) [μs] [a, b]	40
Φ_{PL} (300 K) [%] [a]	1
k_r (300 K) [s^{-1}] [c]	2.5×10^2
k_{nr} (300 K) [s^{-1}] [d]	2.5×10^4
Chromaticity (300 K) [x, y] [a, e]	0.429, 0.492
λ_{max} (77 K) [nm] [a]	518
τ (77 K) [μs] [a, b]	304
Φ_{PL} (77 K) [%] [a]	14
k_r (77 K) [s^{-1}] [c]	4.6×10^2
k_{nr} (77 K) [s^{-1}] [d]	2.8×10^3
Chromaticity (77 K) [x, y] [a, e]	0.268, 0.704
ΔE [cm^{-1}]/[meV]	280/35
$10Dq_{tet}$ [cm^{-1}]	1810
B [cm^{-1}]	634
$E_1^{dir}(0)$ [cm^{-1}]/[eV]	16,777/2.08
$E_2^{dir}(0)$ [cm^{-1}]/[eV]	24,279/3.01
$E_2^{indir}(0)$ [cm^{-1}]/[eV]	20,488/2.54

[a] Excitation wavelength is λ_{Ex} = 455 nm; [b] emission wavelength is λ_{Em} = 538 nm; [c] radiative decay rate: $k_r = \Phi_{PL}/\tau$; [d] non-radiative decay rate: $k_{nr} = \tau^{-1} - k_r$; [e] CIE 1931 color space.

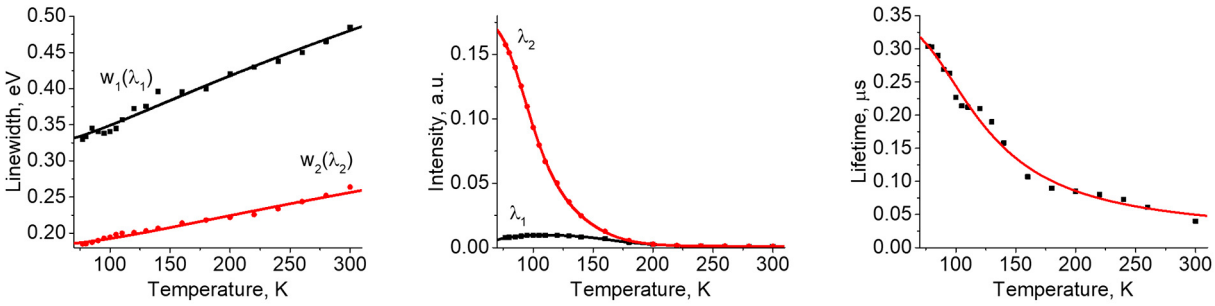

Figure 3. Temperature dependences of the (**a**) photoluminescence linewidth, (**b**) intensity, and (**c**) lifetime (λ_{Ex} = 455 nm and λ_{Em} = 538 nm) of (**1**).

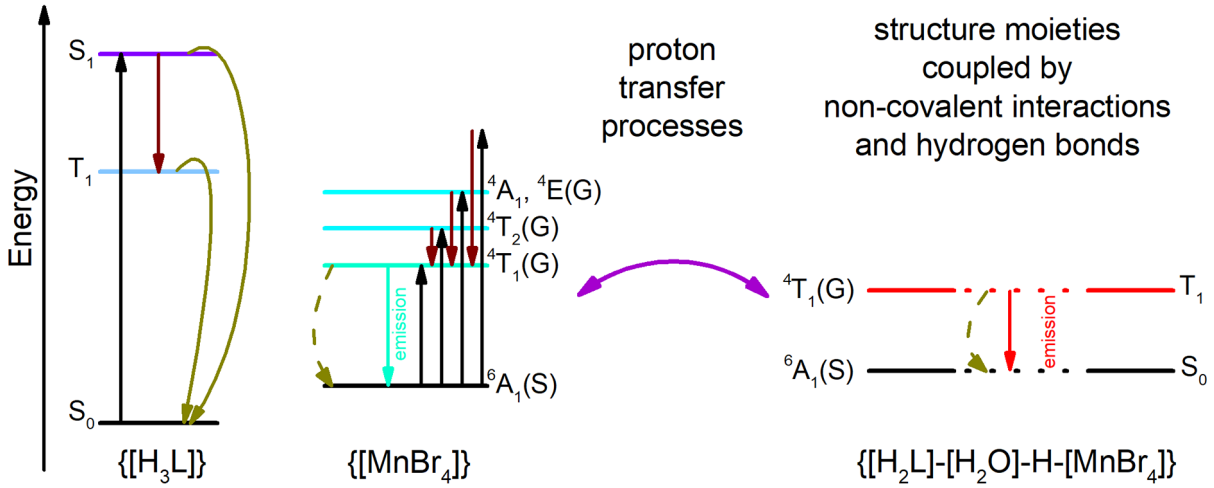

Figure 4. Representation of energy transfer and emission processes in **1** (—: absorption, —: internal conversion and intersystem crossing transition, —: emission of an uncoupled {[$MnBr_4$]} moiety, —: proton transfer processes, —: emission of a coupled {[H_2L]-[H_2O]-H-[$MnBr_4$]} moiety, and —: non-radiative relaxation).

3.3. Optics

The analysis of the temperature dependence of the absorption spectra $\alpha(h\vartheta)$ (obtained by the Kubelka–Munk method (Figures S5 and S6)) using Tauc plots indicates different types of band–band transitions. The direct band–band transition was estimated from the $(\alpha \cdot h\vartheta)^2$ Tauc plot by the following equation [62]:

$$E_i^{dir}(T) = E_i^{dir}(0) - 2 * S_i^{dir} * E_p^{dir} * \left(\coth\left(\frac{E_p^{dir}}{k_B * T} \right) - 1 \right),$$

where $E_2^{dir}(0)$ is band gap energy at $T = 0$, with $E_2^{dir}(0) \approx 3.01$ eV, $S_2^{dir} \approx 3$, and $E_{p2}^{dir} \approx 30$ meV (Figure 5). In addition, analysis of the $(\alpha \cdot h\vartheta)^{1/2}$ Tauc plot (Figure S6) gives the indirect band–band transition energy value of $E_2^{indir} \approx 2.54$ eV with $E_p^{indir} \approx 310$ meV ($E_2^{indir} + E_p^{indir} \approx 2.85$ eV). It should be noted that there is a slight slope of the $(\alpha \cdot h\vartheta)^2$ Tauc plot in the low-energy range (Figure S6). This slope may be associated with either the additional low-energy direct band–band transition with parameters $E_1^{dir}(0) \approx 2.08$ eV, $S_1^{dir} \approx 5$, and $E_{p1}^{dir} \approx 30$ meV (Figure 5) or with the Urbach edge. Taking into account quantum chemical calculations (see below), the presence of a low-intensity direct band–band transition can be assumed.

Quantum-chemical calculations were carried out for a deeper investigation of the nature of the absorption and two-band luminescence. Compound **1** has several intra- and intermolecular hydrogen bonds which can provide the proton transfer. The {MnBr . . . HO} and {HO . . . HO} interactions were investigated in detail. The 3D potential energy surface of the ground state was calculated along the {MnBr . . . HO} and {HO . . . HO} vibrations. The calculation shows the presence of the two minima (Figure 5). The transition energies corresponding to the charge transfer from bromide to manganese ion for global and local minima are $\Delta E_{global} \approx 3.02$ eV and $\Delta E_{local} \approx 2.82$ eV, respectively. These values are in good agreement with $E_2^{dir}(0)$ and $\Delta E_2^{indir} + E_p^{indir}$, respectively. It should be noted that the global and local minima are separated by a barrier with energies $\Delta E_{ground}^{forward} \approx 420$ meV and $\Delta E_{ground}^{backward} \approx 110$ meV, on the one hand, and $\Delta E_{excited}^{forward} \approx 340$ meV and $\Delta E_{excited}^{backward} \approx 110$ meV, on the other, for ground and excited states, respectively. The transition energies corresponding to the charge transfer from bromide to the organic cation for global and local minima were additionally calculated to be $\Delta E_{global}^{low-energy} \approx 2.08$ eV and $\Delta E_{local}^{low-energy} \approx 1.81$ eV, respec-

tively. The oscillator strength of the transfer transition to the organic cation is approximately 10 times lower than for the charge transfer to the manganese ion.

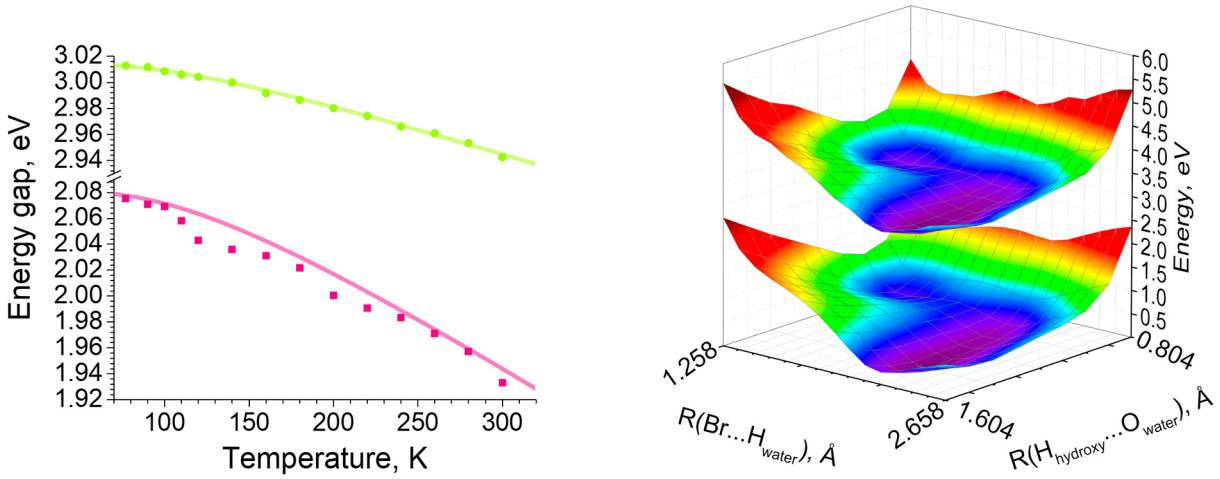

(**a**) (**b**)

Figure 5. (**a**) Temperature dependence of the bandgap energies of **1**, and (**b**) calculated potential energy surfaces of the ground and excited states of **1** along the R(Br ... H_{water}) and R($H_{hydroxy}$ ... O_{water}) distance changing.

Calculated spin-flip transitions between different *d*-orbitals of manganese(II) ion from the global minimum point have energies about $\lambda_{SF}^{Ex_1}$ = 481 nm (2.58 eV), $\lambda_{SF}^{Ex_2}$ = 462 nm (2.69 eV), and $\lambda_{SF}^{Ex_3}$ = 431 nm (2.88 eV) that are close to luminescence excitation values. The first spin-flip transition from the local minimum point has an energy of about $\lambda_{SF}^{Ex_1}$ = 602 nm (2.06 eV) and involves not only *d*-orbitals of manganese(II), but also *p*-orbitals of carbon and nitrogen atoms and *s*-orbitals of hydrogen atoms. This indicates the coupling between all fragments of **1** through noncovalent interactions and hydrogen bonds.

The calculated phonon structure (Figure S11) shows that the phonons with energies 300–450 meV (DFT calculated $\Delta E^{forward}$ and absorption data E_p^{indir}) correspond to the proton vibrations of NH ... O and OH ... O groups (Figures S12–S15). Therefore, the observed indirect band–band transition can be attributed to the phonon-assistance excitation accompanied by the proton transfer. The phonons with energies ~25–40 meV (absorption data E_{p1}^{dir} and E_{p2}^{dir}, luminescence linewidth data E_{p_1} and E_{p_2}, and luminescence intensity data $\Delta E_{\lambda_1 pop}$ and $\Delta E_{\lambda_2 depop_1}$) correspond to the vibrations of the {$[MnBr_4]^{2-}$} fragment (Figure S13). It was found that the bromide and manganese(II) ions are involved in both luminescence bands as well as in both direct absorption processes.

3.4. EPR

The EPR spectrum measured for compound **1** (Figure 6) represents distorted single lines with a peak-to-peak linewidth of ΔH_{pp} = 32.7 mT. To fit such a spectrum, the model typical of $[MnBr_4]^{2+}$ [26,27] was proposed in the form of a paramagnetic center with electron spin $S = 5/2$ accompanied by zero-field splitting. In this case, the following spin Hamiltonian formula can be used:

$$\hat{H} = \beta \hat{\boldsymbol{S}} \boldsymbol{g} \boldsymbol{H} + \hat{\boldsymbol{S}} \boldsymbol{D} \hat{\boldsymbol{S}}$$

where β is a Bohr magneton, $\boldsymbol{g}$ is a g-tensor, $\boldsymbol{D}$ is a zero-field splitting tensor, and $\boldsymbol{H}$ is a magnetic field. Conventionally, the tensor $\boldsymbol{D}$ is expressed through the parameters $D = \frac{3}{2} D_{zz}$ and $E = \frac{D_{xx} - D_{yy}}{2}$ and these will be used below. To reduce the number of varying parameters in the fitting procedure, the typical approximation for manganese(II) compounds of the isotropic g-tensor with ignored Mn(II) hyperfine interaction has been chosen. The

experimental g-factor value was estimated to be g = 2.013. Exploiting the least-squares fitting technique implemented in the EasySpin program package, a spectrum was obtained which corresponds to the experimental one rather well (Figure 6). The resulting experimental EPR parameters are given in Table 2. The concentration of the Mn(II) ions evaluated by the EPR technique—with $CuSO_4$ $5H_2O$ standard being $9.6 \cdot 10^{20}$ paramagnetic centers with $S = 5/2$ per gram—is in good agreement with the theoretical value $9.9 \cdot 10^{20}$ (97%).

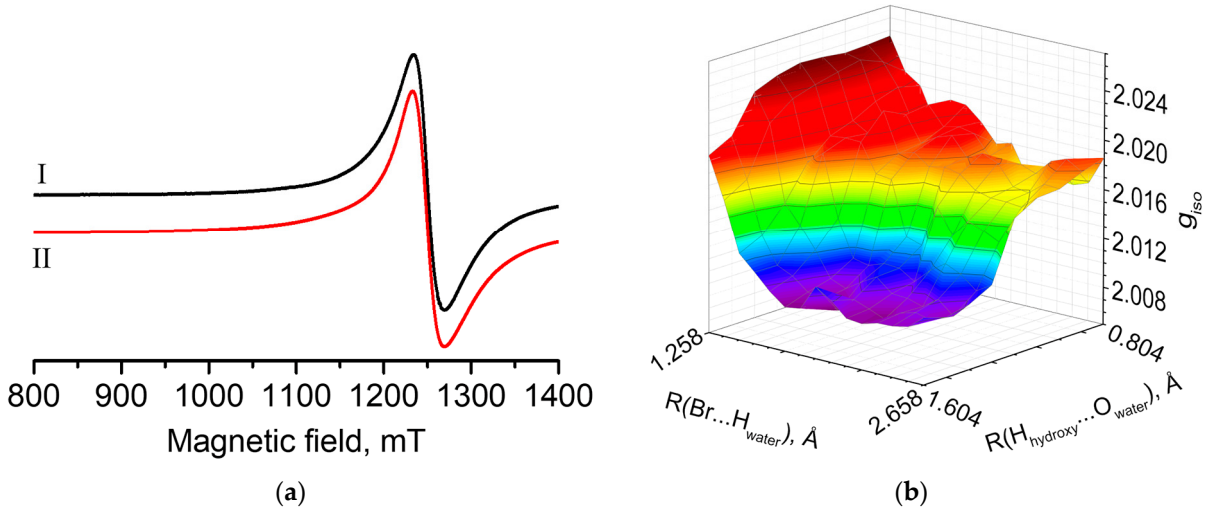

(**a**) (**b**)

Figure 6. (**a**) EPR spectra of **1**, experimental (I) and as best fit of the experimental data (II) and (**b**) calculated ***g***–tensor values along the ground state potential energy surface of **1**.

Table 2. Experimental and DFT calculated EPR parameters.

	***g*-Tensor**	**$\|D\|$ and $\|E\|/\|D\|$**
Experimental	g = 2.013	D = 2430 MHz E/D = 0.03
Calculated Global minimum point	g_{xx} = 2.007 g_{yy} = 2.010 g_{zz} = 2.012 g_{iso} = 2.010	D = 2285 MHz E/D = 0.09
Calculated Local minimum point	g_{xx} = 2.010 g_{yy} = 2.015 g_{zz} = 2.032 g_{iso} = 2.019	D = 4056 MHz E/D = 0.32

Quantum chemical calculations have been performed to check the correctness of the spectrum analysis. The calculated ***g***- and ***D***-tensor eigenvalues are close to that experimentally determined, which indicates that the model for the paramagnetic center has been chosen correctly. In view of the two minima in the potential energy surface for **1** (Figure 6), it should be mentioned that the straightforward description of the experimental spectrum as a sum of two single lines with different isotropic g-tensors was tested and did not result in any increase in the similarity between calculated and measured spectra. In such a case, it can be assumed that the ***g***- and ***D***-tensors of **1** are predominantly determined by the global state of the compound, whereas the possibility of proton transfers leads to the broadening of the EPR spectrum.

4. Conclusions

The luminescent organic–inorganic cation–anion tetrabromomanganate(II) compound with diprotonated 1-hydroxy-2-(pyridin-2-yl)-4,5,6,7-tetrahydrobenzimidazole has been synthesized and investigated. The crystal structure of the compound contains a few pathways for O ... HN, Br ... HO, and O ... HO proton transfers. The interligand proton transfers play an important role in the observed luminescence, optical, and magnetic properties. The ground state of the Mn(II) ion is an orbital singlet $^6\mathbf{S}_{5/2}$ ($^6A_1$) according to the EPR data. The processes of the proton transfer result in the broadening of the EPR spectrum. The compound manifests two-band luminescence. The high energy luminescence band is caused by the $^4T_1(\mathbf{G})\rightarrow{}^6A_1(\mathbf{S})$ transition of the manganese(II) ion. The low energy luminescence band is thought to be caused by the transitions from the triplet state of organic cation and the *d*-orbitals of manganese(II). These states are coupled through {[H_2L]}-{[$MnBr_4$]}-{[H_2O]} vibrations. The luminescence, optical, and magnetic properties of organic-inorganic manganese(II) compounds are closely associated with these proton transfers.

Supplementary Materials: The following supporting information can be downloaded at: https://www.mdpi.com/article/10.3390/inorganics10120245/s1: Crystallographic data, X-ray powder diffraction data, IR spectra, calorimetric data, Absorption data, Luminescence chromaticity data, and DFT calculation data.

Author Contributions: A.S.B.: investigation, data curation, project administration, and writing—review and editing. A.D.: formal analysis, and methodology. A.S.: investigation, and writing—review and editing. B.S.: formal analysis. A.K.: investigation, data curation, and writing—review and editing. All authors have read and agreed to the published version of the manuscript.

Funding: Ministry of Science and Higher Education of the Russian Federation No. 121031700313-8 and AAAA-A21-121011490017-5, RF President Grant MK-5375.2022.1.3.

Data Availability Statement: Not applicable.

Conflicts of Interest: There is no conflict to declare.

References

1. Li, W.; Liu, L.; Tan, M.; He, Y.; Guo, C.; Zhang, H.; Wei, H.; Yang, B. Low-Cost and Large-Area Hybrid X-ray Detectors Combining Direct Perovskite Semiconductor and Indirect Scintillator. *Adv. Funct. Mater.* **2021**, *31*, 2107843. [CrossRef]
2. Tan, L.; Luo, Z.; Chang, X.; Wei, Y.; Tang, M.; Chen, W.; Li, Q.; Shen, P.; Quan, Z. Structure and Photoluminescence Transformation in Hybrid Manganese(II) Chlorides. *Inorg. Chem.* **2021**, *60*, 6600–6606. [CrossRef] [PubMed]
3. Hausmann, D.; Kuzmanoskia, A.; Feldmann, C. MnBr2/18-crown-6 coordination complexes showing high room temperature luminescence and quantum yield. *Dalton Trans.* **2016**, *45*, 6541–6547. [CrossRef]
4. Peng, H.; Zou, B.; Guo, Y.; Xiao, Y.; Zhi, R.; Fan, X.; Zou, M.; Wang, J. Evolution of the structure and properties of mechanochemically synthesized pyrrolidine incorporated manganese bromide powders. *J. Mater. Chem. C* **2020**, *8*, 6488–6495. [CrossRef]
5. Zhou, G.; Ding, J.; Jiang, X.; Zhang, J.; Molokeev, M.S.; Ren, Q.; Zhou, J.; Li, S.; Zhang, X.-M. Coordination units of Mn2+ modulation toward tunable emission in zero-dimensional bromides for white light-emitting diodes. *J. Mater. Chem. C* **2022**, *10*, 2095–2102. [CrossRef]
6. Chen, J.; Zhang, S.; Pan, X.; Li, R.; Ye, S.; Cheetham, A.K.; Mao, L. Structural Origin of Enhanced Circularly Polarized Luminescence in Hybrid Manganese Bromides. *Angew. Chem. Int. Ed.* **2022**, *61*, e202205906. [CrossRef]
7. Zhao, J.; Zhang, T.; Dong, X.Y.; Sun, M.E.; Zhang, C.; Li, X.; Zhao, Y.S.; Zang, S.Q. Circularly Polarized Luminescence from Achiral Single Crystals of Hybrid Manganese Halides. *J. Am. Chem. Soc.* **2019**, *141*, 15755–15760. [CrossRef]
8. Xuan, H.L.; Sang, Y.F.; Xu, L.J.; Zheng, D.S.; Shi, C.M.; Chen, Z.N. Amino-Acid-Induced Circular Polarized Luminescence in One-Dimensional Manganese(II) Halide Hybrid. *Chem. A Eur. J.* **2022**, *28*, e202201299. [CrossRef]
9. Qin, Y.; She, P.; Huang, X.; Huang, W.; Zhao, Q. Luminescent manganese(II) complexes: Synthesis, properties and optoelectronic applications. *Coord. Chem. Rev.* **2020**, *416*, 213331. [CrossRef]
10. Croitor, L.; Cocu, M.; Bulhac, I.; Bourosh, P.N.; Kravtsov, C.V.; Petuhov, O.; Danilescu, O. Evolution from discrete mononuclear complexes to trinuclear linear cluster and 2D coordination polymers of Mn(II) with dihydrazone Schiff bases: Preparation, structure and thermal behavior. *Polyhedron* **2021**, *206*, 115329. [CrossRef]
11. Ma, C.; Wang, W.; Zhang, X.; Chen, C.; Liu, Q.; Zhu, H.; Liao, D.; Li, L.; Cano, J.; Demunno, G.; et al. Molecular, one- and two-dimensional systems built from manganese(II) and phthalate/diimine ligands: Syntheses, crystal structures and magnetic properties. *Eur. J. Inorg. Chem.* **2004**, *17*, 3522–3532. [CrossRef]

12. Bikas, R.; Karimian, R.; Siczek, M.; Demeshko, S.; Hosseini-Monfared, H.; Lis, T. Magnetic and spectroscopic properties of a 2D Mn(II) coordination polymer with carbohydrazone ligand. *Inorg. Chem. Commun.* **2016**, *70*, 219–222. [CrossRef]
13. Chen, S.; Gao, J.; Chang, J.; Zhang, Y.; Feng, L. Organic-inorganic manganese (II) halide hybrids based paper sensor for the fluorometric determination of pesticide ferbam. *Sens. Actuators B Chem.* **2019**, *297*, 126701. [CrossRef]
14. Smirnov, V.I.; Sinegovskaya, L.M.; Parshina, L.N.; Artem'ev, A.V.; Sterkhova, I.V. Copper(II), cobalt(II), manganese(II) and nickel(II) bis(hexafluoroacetylacetonate) complexes with N-vinylimidazole. *Mendeleev Commun.* **2020**, *30*, 246–248. [CrossRef]
15. Davydova, M.P.; Bauer, I.A.; Brel, V.K.; Rakhmanova, M.I.; Bagryanskaya, I.Y.; Artem'ev, A.V. Manganese(II) Thiocyanate Complexes with Bis(phosphine Oxide) Ligands: Synthesis and Excitation Wavelength-Dependent Multicolor Luminescence. *Eur. J. Inorg. Chem.* **2020**, *2020*, 695–703. [CrossRef]
16. Tao, P.; Liu, S.J.; Wong, W.Y. Phosphorescent Manganese(II) Complexes and Their Emerging Applications. *Adv. Opt. Mater.* **2020**, *8*, 2000985. [CrossRef]
17. Meng, H.; Zhu, W.; Li, F.; Huang, X.; Qin, Y.; Liu, S.; Yang, Y.; Huang, W.; Zhao, Q. Highly Emissive and Stable Five-Coordinated Manganese(II) Complex for X-ray Imaging. *Laser Photonics Rev.* **2021**, *15*, 2100309. [CrossRef]
18. Artemev, A.V.; Davydova, M.P.; Berezin, A.S.; Brel, V.K.; Morgalyuk, V.P.; Bagryanskaya, I.Y.; Samsonenko, D.G. Luminescence of the Mn2+ ion in non-: O h and T d coordination environments: The missing case of square pyramid. *Dalton Trans.* **2019**, *48*, 16448–16456. [CrossRef]
19. Berezin, A.S.; Samsonenko, D.G.; Brel, V.K.; Artem'Ev, A.V. "Two-in-one" organic-inorganic hybrid MnII complexes exhibiting dual-emissive phosphorescence. *Dalton Trans.* **2018**, *47*, 7306–7315. [CrossRef]
20. Bortoluzzi, M.; Castro, J.; Gobbo, A.; Ferraro, V.; Pietrobon, L. Light harvesting indolyl-substituted phosphoramide ligand for the enhancement of Mn(ii) luminescence. *Dalton Trans.* **2020**, *49*, 7525–7534. [CrossRef]
21. Berezin, A.S.; Davydova, M.P.; Bagryanskaya, I.Y.; Artyushin, O.I.; Brel, V.K.; Artem'ev, A.V. A red-emitting Mn(II)-based coordination polymer build on 1,2,4,5-tetrakis(diphenylphosphinyl)benzene. *Inorg. Chem. Commun.* **2019**, *107*, 107473. [CrossRef]
22. Vinogradova, K.A.; Shekhovtsov, N.A.; Berezin, A.S.; Sukhikh, T.S.; Krivopalov, V.P.; Nikolaenkova, E.B.; Plokhikh, I.V.; Bushuev, M.B. A near-infra-red emitting manganese(II) complex with a pyrimidine-based ligand. *Inorg. Chem. Commun.* **2019**, *100*, 11–15. [CrossRef]
23. Zhou, Q.; Dolgov, L.; Srivastava, A.M.; Zhou, L.; Wang, Z.; Shi, J.; Dramićanin, M.D.; Brik, M.G.; Wu, M. Mn2+ and Mn4+ red phosphors: Synthesis, luminescence and applications in WLEDs. A review. *J. Mater. Chem. C* **2018**, *6*, 2652–2671. [CrossRef]
24. Berezin, A.S.; Vinogradova, K.A.; Nadolinny, V.A.; Sukhikh, T.S.; Krivopalov, V.P.; Nikolaenkova, E.B.; Bushuev, M.B. Temperature- and excitation wavelength-dependent emission in a manganese(II) complex. *Dalton Trans.* **2018**, *47*, 1657–1665. [CrossRef]
25. Bortoluzzi, M.; Castro, J.; Ferraro, V. Dual emission from Mn(II) complexes with carbazolyl-substituted phosphoramides. *Inorg. Chim. Acta* **2022**, *536*, 120896. [CrossRef]
26. Berezin, A.S. A halomanganates(Ii) with p,p'-diprotonated bis(2-diphenylphosphinophenyl)ether: Wavelength-excitation dependence of the quantum yield and role of the non-covalent interactions. *Int. J. Mol. Sci.* **2021**, *22*, 6873. [CrossRef] [PubMed]
27. Berezin, A.S. A brightly emissive halomanganates(II) with triphenylphosphonium cation: Synthesis, luminescence, and up-conversion phenomena. *Dye. Pigment.* **2021**, *196*, 109782. [CrossRef]
28. Berezin, A.S.; Vinogradova, K.A.; Krivopalov, V.P.; Nikolaenkova, E.B.; Plyusnin, V.F.; Kupryakov, A.S.; Pervukhina, N.V.; Naumov, D.Y.; Bushuev, M.B. Excitation-Wavelength-Dependent Emission and Delayed Fluorescence in a Proton-Transfer System. *Chem. A Eur. J.* **2018**, *24*, 12790–12795. [CrossRef]
29. Behera, S.K.; Park, S.Y.; Gierschner, J. Dual Emission: Classes, Mechanisms, and Conditions. *Angew. Chem. Int. Ed.* **2021**, *60*, 22624–22638. [CrossRef]
30. Shekhovtsov, N.A.; Nikolaenkova, E.B.; Berezin, A.S.; Plyusnin, V.F.; Vinogradova, K.A.; Naumov, D.Y.; Pervukhina, N.V.; Tikhonov, A.Y.; Bushuev, M.B. A 1-Hydroxy-1H-imidazole ESIPT Emitter Demonstrating anti-Kasha Fluorescence and Direct Excitation of a Tautomeric Form. *ChemPlusChem* **2021**, *86*, 1436–1441. [CrossRef] [PubMed]
31. Komarovskikh, A.; Danilenko, A.; Sukhikh, A.; Syrokvashin, M.; Selivanov, B. Structure and EPR investigation of Cu(II) bifluoride complexes with zwitterionic N-hydroxyimidazole ligands. *Inorg. Chim. Acta* **2020**, *517*, 120187. [CrossRef]
32. Dolomanov, O.V.; Bourhis, L.J.; Gildea, R.J.; Howard, J.A.K.; Puschmann, H. OLEX2: A complete structure solution, refinement and analysis program. *J. Appl. Crystallogr.* **2009**, *42*, 339–341. [CrossRef]
33. *APEX3 (v.2018-7.2)*, Bruker AXS Inc.: Madison, WI, USA, 2018.
34. Sheldrick, G.M. SHELXT—Integrated space-group and crystal-structure determination. *Acta Crystallogr. Sect. A Found. Crystallogr.* **2015**, *A71*, 3–8. [CrossRef] [PubMed]
35. Sheldrick, G.M. Crystal structure refinement with SHELXL. *Acta Crystallogr. Sect. C: Struct. Chem.* **2015**, *C71*, 3–8. [CrossRef]
36. Stoll, S.; Schweiger, A. EasySpin, a comprehensive software package for spectral simulation and analysis in EPR. *J. Magn. Reson.* **2006**, *178*, 42–55. [CrossRef]
37. Te Velde, G.; Bickelhaupt, F.M.; Baerends, E.J.; Fonseca Guerra, C.; van Gisbergen, S.J.A.; Snijders, J.G.; Ziegler, T. Chemistry with ADF. *J. Comput. Chem.* **2001**, *22*, 931–967. [CrossRef]
38. ADF2021. *SCM, Theoretical Chemistry*; Vrije Universiteit: Amsterdam, The Netherlands, 2021; Available online: http://www.scm.com (accessed on 1 October 2021).
39. Perdew, J.P. Density-functional approximation for the correlation energy of the inhomogeneous electron gas. *Phys. Rev. B* **1986**, *33*, 8822, Erratum in *Phys. Rev. B* **1986**, *34*, 7406. [CrossRef]

40. Becke, A.D. Density-functional exchange-energy approximation with correct asymptotic behavior. *Phys. Rev. A* **1988**, *38*, 3098–3100. [CrossRef]
41. Van Lenthe, E.; Baerends, E.J.; Snijders, J.G. Relativistic regular two-component Hamiltonians. *J. Chem. Phys.* **1993**, *99*, 4597–4610. [CrossRef]
42. Van Lenthe, E.; Baerends, E.J.; Snijders, J.G. Relativistic total energy using regular approximations. *J. Chem. Phys.* **1994**, *101*, 9783–9792. [CrossRef]
43. Van Lenthe, E. Geometry optimizations in the zero order regular approximation for relativistic effects. *J. Chem. Phys.* **1999**, *110*, 8943–8953. [CrossRef]
44. Van Lenthe, E.; Wormer, P.E.S.; Van Der Avoird, A. Density functional calculations of molecular g-tensors in the zero-order regular approximation for relativistic effects. *J. Chem. Phys.* **1997**, *107*, 2488–2498. [CrossRef]
45. Grimme, S. Accurate description of van der Waals complexes by density functional theory including empirical corrections. *J. Comput. Chem.* **2004**, *25*, 1463–1473. [CrossRef]
46. Ernzerhof, M.; Scuseria, G.E. Assessment of the Perdew-Burke-Ernzerhof exchange-correlation functional. *J. Chem. Phys.* **1999**, *110*, 5029–5036. [CrossRef]
47. Van Gisbergen, S.J.A.; Snijders, J.G.; Baerends, E.J. Implementation of time-dependent density functional response equations. *Comput. Phys. Commun.* **1999**, *118*, 119–138. [CrossRef]
48. Wang, F.; Ziegler, T. A simplified relativistic time-dependent density-functional theory formalism for the calculations of excitation energies including spin-orbit coupling effect. *J. Chem. Phys.* **2005**, *123*, 154102. [CrossRef]
49. Yanai, T.; Tew, D.P.; Handy, N.C. A new hybrid exchange-correlation functional using the Coulomb-attenuating method (CAM-B3LYP). *Chem. Phys. Lett.* **2004**, *393*, 51–57. [CrossRef]
50. Wang, F.; Ziegler, T. Time-dependent density functional theory based on a noncollinear formulation of the exchange-correlation potential. *J. Chem. Phys.* **2004**, *121*, 12191–12196. [CrossRef]
51. Wang, F.; Ziegler, T. The performance of time-dependent density functional theory based on a noncollinear exchange-correlation potential in the calculations of excitation energies. *J. Chem. Phys.* **2005**, *122*, 074109. [CrossRef]
52. Riplinger, C.; Kao, J.P.Y.; Rosen, G.M.; Kathirvelu, V.; Eaton, G.R.; Eaton, S.S.; Kutateladze, A.; Neese, F. Interaction of radical pairs through-bond and through-space: Scope and limitations of the point-dipole approximation in electron paramagnetic resonance spectroscopy. *J. Am. Chem. Soc.* **2009**, *131*, 10092–10106. [CrossRef]
53. Neese, F. Calculation of the zero-field splitting tensor on the basis of hybrid density functional and Hartree-Fock theory. *J. Chem. Phys.* **2007**, *127*, 164112. [CrossRef] [PubMed]
54. Neese, F. The ORCA program system. *Wiley Interdiscip. Rev. Comput. Mol. Sci.* **2012**, *2*, 73–78. [CrossRef]
55. Neese, F. *ORCA—An ab Initio, DFT and Semiempirical SCF-MO Package*, Version 5.0; Max Planck Institute: Mulheim, Germany, 2021.
56. Komarovskikh, A.; Uvarov, M.; Nadolinny, V.; Palyanov, Y. Spin Relaxation of the Neutral Germanium-Vacancy Center in Diamond. *Phys. Status Solidi A Appl. Mater. Sci.* **2018**, *215*, 1800193. [CrossRef]
57. Heß, B.A.; Marian, C.M.; Wahlgren, U.; Gropen, O. A mean-field spin-orbit method applicable to correlated wavefunctions. *Chem. Phys. Lett.* **1996**, *251*, 365–371. [CrossRef]
58. Adamo, C.; Barone, V. Toward reliable density functional methods without adjustable parameters: The PBE0 model. *J. Chem. Phys.* **1999**, *110*, 6158–6170. [CrossRef]
59. Weigend, F.; Ahlrichs, R. Balanced basis sets of split valence, triple zeta valence and quadruple zeta valence quality for H to Rn: Design and assessment of accuracy. *Phys. Chem. Chem. Phys.* **2005**, *7*, 3297–3305. [CrossRef]
60. Zhang, S.; Zhao, Y.; Zhou, J.; Ming, H.; Wang, C.H.; Jing, X.; Ye, S.; Zhang, Q. Structural design enables highly-efficient green emission with preferable blue light excitation from zero-dimensional manganese (II) hybrids. *Chem. Eng. J.* **2021**, *421*, 129886. [CrossRef]
61. Tanabe, Y.; Sugano, S. On the Absorption Spectra of Complex Ions. *J. Phys. Soc. Jpn.* **1954**, *9*, 753–766. [CrossRef]
62. Zhou, P.; Zhang, X.; Li, L.; Liu, X.; Yuan, L.; Zhang, X. Temperature-dependent photoluminescence properties of Mn:ZnCuInS nanocrystals. *Opt. Mater. Express* **2015**, *5*, 2069–2080. [CrossRef]